京都大学防災研究所年報 第 50 号 B 平成 19 年 4 月
Annuals of Disas. Prev. Res. Inst., Kyoto Univ., No. 50 B, 2007

Morphodynamics of Channels with Groins and its Application in River Restoration

Hao ZHANG, Hajime NAKAGAWA, Yasunori MUTO, Yoshio MURAMOTO*, Daizaburou TOUCHI**and Yasunori NANBU**

* Professor Emeritus of Kyoto University
** Graduate School of Engineering, Kyoto University

Synopsis

This study investigates the flow and bed deformation process in a channel with groins in a river restoration project using both physical model experiment and numerical simulation methods. The experiment is based on a large-scale physical model and is able to resolve the local flow and sediment transport phenomena with a relatively high accuracy. The numerical model is formulated on unstructured meshes and allows the exact representation of complex geometries commonly encountered in the engineering practice. The numerical results have been compared with those of the experimental measurements. Reasonable agreements have been obtained in terms of both flow patterns and bed variations.

Keywords: channel morphodynamics, groin, river restoration, large-scale physical model, complex geometry, unstructured mesh

1. Introduction

In-stream structures such as groins have been widely used in the river engineering to restore channel morphologies and improve aquatic habitats. Compared with other restoration structures such as bank covers and weirs, groins have been documented to be the most durable solution (Shields, et al., 1995). Consequently, investigations on the flow and/or bed deformation around groins have been carried out, in the past several decades, by a lot of researchers with field surveys, laboratorial experiments and numerical simulations, e.g. Kuhnle et al. (2002), Muto et al. (2003), Sukhodolov et al. (2004) and Nagata et al. (2005). These studies provide a substantial collection of data and information on the flow and sediment transport around this typical kind of in-stream structures. However, existing research results are usually problem-dependent and have not been developed yet up to practical knowledge for the design of restoration projects. Although there do exist some design suggestions and recommendations based on one or several researches for river restoration projects, the complexities of the real river conditions have been seldom taken into account in a cost-effective way. Approaches based on trial-and-error and limited experiences still play an important role in the state-of-the-art for restoration designs and management in practice. Without a full understanding of the channel hydraulics and morphodynamics caused by restoration measures, many projects have failed in the early stage of their design working life or have been confirmed to be unsustainable. The low success rates usually implicate a loss or a require of a huge amount of investments as well as potential disasters for the riverine eco-system and people living nearby. Therefore, it is necessary to develop more general design methods based on an insight into the underlying physics of the problem.

This study investigates the channel morphodynamics before/after the installation of groins and seeks practicable design methods for river restoration. In order to fulfill these tasks, a real restoration project in west Japan has been selected as a reference. The field site of

the project is in the Yodo River- Lake Biwa basin in west Japan and located at the Kizu River about 6km upstream from the confluence where three major rivers, i.e. the Uji River, the Katsura River and the Kizu River, joint together (Fig. 1).

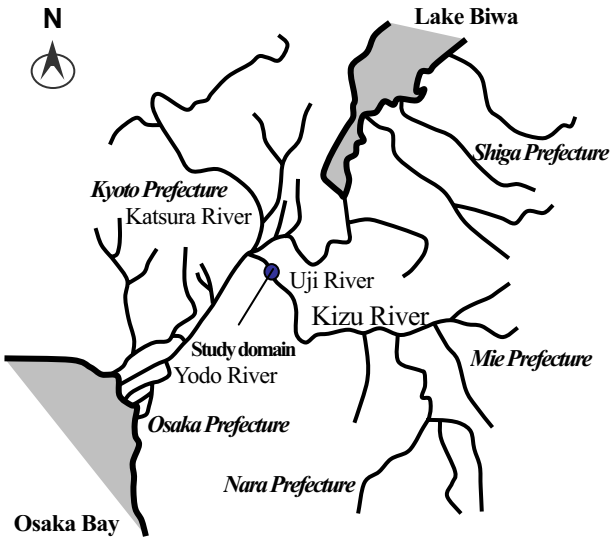

Fig.1 Yodo River-Lake Biwa basin and the study domain

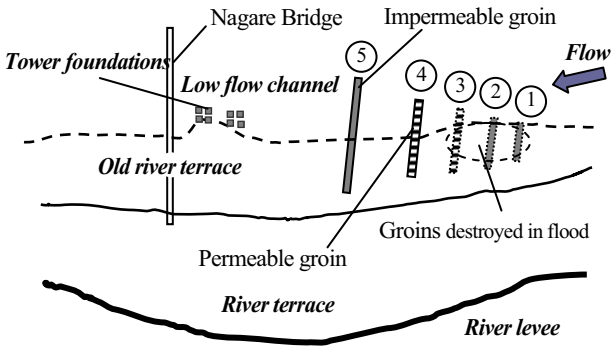

Fig.2 Sketch of the restoration project

The project was built around an ancient wooden bridge: the Nagare Bridge, which is one of the most attractive sightseeing and recreation spots in this river basin. The main objectives are to restore beach landscapes and improve the riparian ecotones around the bridge. Restoration measures mainly include cutting down part of the river terrace and constructing 3 groins (①, ② and ③) as shown in Fig. 2. The project was not successful. It was completed in 2004 but soon failed in a typhoon-induced flood. The 3 groins (one permeable and two impermeable) were almost washed away. As a remedy, a permeable groin (④) and an impermeable groin (⑤) were introduced in the next year after a quick investigation of the effects of the two groins on the riparian restoration. Up to now, the project has been working well. However, the knowledge is still very poor on the river morphodynamics caused by these restoration actions. Intensive studies and long-term monitoring are still of great necessity.

Both large-scale physical model experiments and 2D numerical simulations have been carried out. The physical model is non-distorted and represents the details of local hydraulic structures to scale in the area of interest, which is able to resolve the local flow and sediment transport phenomena with a relatively high accuracy. The numerical model solves the depth-averaged shallow water equations for the mean flow velocities considering the effect of secondary flows. The bed deformation is obtained by solving the sediment continuity equation in the bedload layer and the sediment transport rate is evaluated with a deterministic empirical formula. The influence of the local bed slope on bedload transport has been taken into account, as well as the deviation of the near-bed flow direction from that of the mean flow. Furthermore, the 2D model is formulated on an unstructured mesh, which allows the exact representation of complex geometries such as the irregular bank-lines and groin structures. Selected numerical results are compared with those of the experimental measurements. Discussions and conclusions are made based on typical velocity fields and bed deformations under various conditions such as the changing of discharges and installing/removing groins.

2. Physical model experiments

The physical model was constructed in the Ujigawa Open Laboratory, Kyoto University (Fig. 3). The model had a physical scale of 1:65 and represented the river reach from section 4.4km to section 7.4km (here km stands for the distance in kilometer from the river confluence as shown in Fig. 1). Local hydraulic structures in the neighborhood of the Nagare Bridge have been exactly represented, including the piers of the bridge, different kinds of groin structures, etc.

Along the transverse section, the river consisted of a low flow channel with a floodplain on either side. The floodplain area was treated as fixed bed and artificial grass was made in some area to model the vegetated area such as the tea fields. The low flow channel was movable and was covered with powdered anthracite after a comprehensive comparison with some other model

sediment materials. The model sediment had a mean diameter of 0.83mm and a specific gravity of 1.41. The sieve analysis result of the sediment samples taken at typical cross-sections on site and the model sediment is shown in Fig. 4.

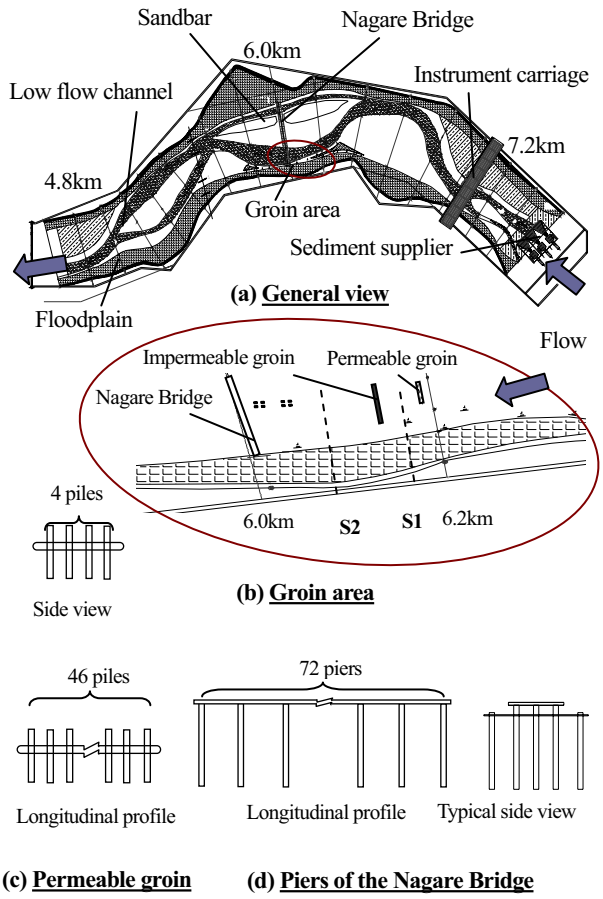

Fig.3 Physical model experimental setup

Continuous sediment supply was guaranteed during the experiments with an automatic sediment supplier installed at the inlet boundary. At the outlet boundary, a tailgate was used to control the water level. At section 4.6km, a point gauge was set to record the downstream water stage. Water level and bed elevation were measured at typical transverse sections during the experiments. In the proximity of the groins, the longitudinal distance between two measured sections was around 10cm (about 6.5m in prototype). The water level was measured with an ultrasonic level system (10s-sampling for a point at a frequency of 100Hz) and the bed elevation was obtained through a sand-surface profiler. The surface flow structure in the groin stretch was studied with PIV (Particle Image Velocimetry) method (30s-sampling for a point at a frequency of 6Hz).

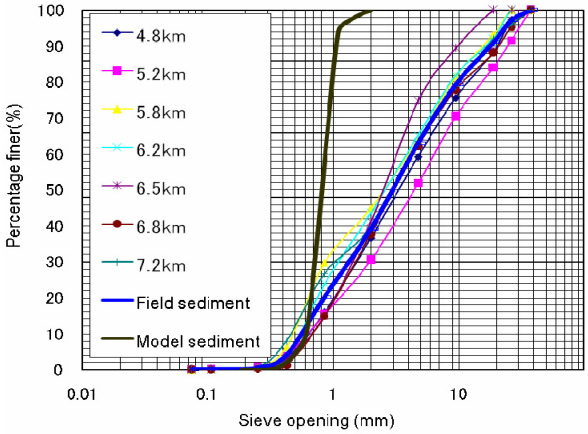

Fig.4 Sieve analysis result of sediment particles

The experimental studies last some 2 years and were conducted in 4 phases one by one:

Phase 1: Preliminary experiments to quantify some important hydraulic parameters such as sediment transport rate and bed roughness in the model channel. Detailed reports were given in Touchi (2006) and Zhang et al. (2006). It has to be mentioned that the sediment transport rates (mainly in bedload mode) to maintain the dynamic equilibrium bed conditions under representative water discharges have been investigated. According to the experimental results, the sediment transport rates under equilibrium conditions were about 70% of those estimated with the widely used Ashida-Michiue formula (Ashida and Michiue, 1972) for Japanese rivers.

Phase 2: Experiments to test the performance of the model channel, i.e. to what extent, the experimental channel might reproduce the flow and sediment transport phenomena in the real river. A 7-year fluvial process and a one-year bed deformation process (considering the effects of the detailed flood process) have been investigated, respectively. The experimental results have been compared with the field data and reasonable agreements have been obtained. Detailed information was reported in Nanbu (2007).

Phase 3: Experiments to investigate the effects of the existing restoration project on channel morphologies. Under the same scenarios for flow and sediment discharges, experiments with groins and without groins were carried out, respectively. Based on the experimental data, together with corresponding numerical simulation results, the performance of the existing groin structures was assessed. It was found that the current restoration measures seemed not enough to fulfill the ultimate goals. Therefore, some actions should be taken to improve the

effectiveness of existing groins. Possible improvement alternatives have been proposed after carefully analyses of both experimental and numerical results.

Phase 4: Experiments to investigate and compare different morphological consequences due to different improvement methods. A strong emphasis has been laid on the local bed deformation in the neighborhood of the Nagare Bridge. Numerical simulations were conducted at the same time with the models described below. The best solution was finally selected.

3. Numerical models

A 2D morphological model has been developed to simulate the flow and sediment transport in this study. The model consists of a depth-averaged flow module, a bedload transport module and a bed deformation module. The flow field, sediment transport and bed deformation in the model are coupled and solved in a quasi-steady way, i.e. when one of them is under calculation, the others are considered as unchanged.

3.1 Hydrodynamic module

Integrating the 3D (Three-dimensional) RANS (Reynolds-averaged Navier-Stokes) equations from the riverbed to the free surface, the following equations governing the 2D open channel flow can be derived.

$$\frac{\partial H}{\partial t}+\frac{\partial}{\partial x}(hu)+\frac{\partial}{\partial y}(hv)=0 \tag{1}$$

$$\frac{\partial u}{\partial t}+u\frac{\partial u}{\partial x}+v\frac{\partial u}{\partial y}=-g\frac{\partial H}{\partial x}+\frac{1}{\rho h}\left[\frac{\partial}{\partial x}(h\pi_{xx})+\frac{\partial}{\partial y}(h\pi_{xy})\right]-\frac{\tau_{bx}}{\rho h}+D_{xx}+D_{xy} \tag{2}$$

$$\frac{\partial v}{\partial t}+u\frac{\partial v}{\partial x}+v\frac{\partial v}{\partial y}=-g\frac{\partial H}{\partial y}+\frac{1}{\rho h}\left[\frac{\partial}{\partial x}(h\pi_{yx})+\frac{\partial}{\partial y}(h\pi_{yy})\right]-\frac{\tau_{by}}{\rho h}+D_{yx}+D_{yy} \tag{3}$$

where t= time; H = water stage (i.e. $H = h + z_b$); h = water depth; z_b = bed elevation; x, y= Cartesian coordinate components; u, v = depth-averaged flow velocity components in the x and y directions, respectively; g= gravitational acceleration; ρ = fluid density; τ_{xx}, τ_{xy}, τ_{yx}, τ_{yy} = depth-averaged turbulent stresses; D_{xx}, D_{xy}, D_{yx}, D_{yy} = dispersion terms due to vertical non-uniformities of the mean flow and τ_{bx}, τ_{by} = bottom shear stresses. Strictly speaking, the bottom shear stresses are related to the near-bed flow field rather than the mean flow field. Nevertheless, the influence due to the deviation of the near-bed flow from the mean flow is omitted so far when Eq.2 and Eq.3 are solved, which results in the following expressions:

$$\tau_{bx}=\rho c_f u\sqrt{u^2+v^2} \tag{4}$$

$$\tau_{by}=\rho c_f v\sqrt{u^2+v^2} \tag{5}$$

in which the bottom friction coefficient c_f is related to the Manning's roughness coefficient n by

$$c_f=\frac{n^2 g}{h^{1/3}} \tag{6}$$

From Eq. 4 and Eq. 5, the near-bed shear velocity is immediately obtained as

$$u_*=\sqrt{\frac{\tau_{bx}^2+\tau_{by}^2}{\rho}} \tag{7}$$

It has to be mentioned that the shear stress and shear velocity near the bed are corrected by replacing the mean velocities in Eq. 4 and Eq. 5 with the near-bed velocities when sediment transport rate and direction are estimated.

Approximating the turbulent stresses with Boussinesq's eddy viscosity concept, one has

$$\tau_{ij}=\rho\upsilon_t\left(\frac{\partial u_i}{\partial x_j}+\frac{\partial u_j}{\partial x_i}\right)-\frac{2}{3}k\delta_{ij} \quad (i,j=x,y) \tag{8}$$

where υ_t = eddy viscosity, k = depth-averaged turbulence kinetic energy and δ_{ij} = Kronecker delta.

In a zero-equation model, the eddy viscosity is estimated through

$$\upsilon_t=\frac{\kappa}{6}u_* h \tag{9}$$

where κ = van Karman constant (=0.41). The result of the zero-equation model is used as an input for more advanced models such as a k-ε model. In the k-ε model, the eddy viscosity is a function of the turbulent kinetic energy k and its dissipation rate ε, i.e.

$$\upsilon_t=c_\mu\frac{k^2}{\varepsilon} \tag{10}$$

where c_μ = coefficient and is usually set to be a constant 0.09. The two quantities k and ε are solved from their transport equations as follows, respectively.

$$\frac{\partial k}{\partial t}+u\frac{\partial k}{\partial x}+v\frac{\partial k}{\partial y}=\frac{\partial}{\partial x}\left(\frac{\upsilon_t}{\sigma_k}\frac{\partial k}{\partial x}\right)+\frac{\partial}{\partial y}\left(\frac{\upsilon_t}{\sigma_k}\frac{\partial k}{\partial y}\right)+P_h+P_{kv}-\varepsilon \tag{11}$$

$$\frac{\partial \varepsilon}{\partial t}+u\frac{\partial \varepsilon}{\partial x}+v\frac{\partial \varepsilon}{\partial y}=\frac{\partial}{\partial x}\left(\frac{\upsilon_t}{\sigma_\varepsilon}\frac{\partial \varepsilon}{\partial x}\right)+\frac{\partial}{\partial y}\left(\frac{\upsilon_t}{\sigma_\varepsilon}\frac{\partial \varepsilon}{\partial y}\right)+c_{1\varepsilon}\frac{\varepsilon}{k}P_h+P_{\varepsilon v}-c_{2\varepsilon}\frac{\varepsilon^2}{k} \tag{12}$$

where

$$P_h = \upsilon_t \left[2\left(\frac{\partial u}{\partial x}\right)^2 + 2\left(\frac{\partial v}{\partial y}\right)^2 + \left(\frac{\partial u}{\partial y} + \frac{\partial v}{\partial x}\right)^2 \right]$$

$$P_{kv} = \frac{u_*^3}{h c_f^{1/2}} \qquad P_{\varepsilon v} = \frac{c_{2\varepsilon} c_\mu^{1/2}}{\left(e_* \sigma_t\right)^{1/2} c_f^{3/4}} \frac{u_*^4}{h^2} \tag{13}$$

in which σ_t = Schmidt number expressing the relation between the eddy viscosity and the diffusivity for scalar transport (a value of 1.0 is adopted in this study) and e_* = adjustable dimensionless diffusivity. The model parameters generally take the following values as suggested by Rodi (1980).

$$\sigma_k = 1.0 \quad \sigma_\varepsilon = 1.3 \quad C_{1\varepsilon} = 1.44 \quad C_{2\varepsilon} = 1.92 \tag{14}$$

During the depth-averaging of the 3D RANS equations, the dispersion terms D_{xx}, D_{xy}, D_{yx}, D_{yy} appear as shown in Eq.2 and Eq.3 (Rodi, 1980). These terms exhibit similar physical effect with the turbulent stresses and can be significant when the secondary flow is obvious. Minh Duc et al. (2004) suggested to adjust the dimensionless diffusivity coefficient e_* in the k-ε transport equations to indirectly account for secondary flow effects according to their numerical experiments. A value of 0.15 has been suggested for laboratory flumes. In natural rivers, a value from 0.6 up to 10 might be used. Following their idea, the dimensionless diffusivity is treated as an adjustable parameter to include the effect of the secondary flow on the mean flow in this study. In practice, this parameter is firstly tuned by conducting fixed-bed computation. After that, the simulation of movable bed is started.

It is well accepted that the direction and the magnitude of the near-bed velocities do not coincide with those of the mean velocities in natural river conditions. In order to estimate the near-bed velocities, they are resolved into a primary velocity U and a secondary flow velocity V. The former is in the same direction as that of the mean flow, while the latter is normal to the primary velocity and has a magnitude related to the water depth, the primary flow curvature and the primary velocity, i.e.

$$U = a_U \sqrt{u^2 + v^2} \tag{15}$$

$$V = \frac{h}{r} N_* U \tag{16}$$

where a_U = coefficient considering the primary velocity profile in the vertical direction (=1.0 in this study for simplicity); N_* = coefficient representing the intensity of the secondary flow (=7.0 for fully developed bend flows, Engelund, 1974) and r = radius of the curvature of the streamline. According to Shimizu and Itakura (1991), it is estimated from

$$\frac{1}{r} = \frac{1}{\left(u^2 + v^2\right)^{3/2}} \left[u\left(u\frac{\partial v}{\partial x} - v\frac{\partial u}{\partial x}\right) + v\left(u\frac{\partial v}{\partial y} - v\frac{\partial u}{\partial y}\right) \right] \tag{17}$$

3.2 Sediment transport module

In the absence of suspended load, the bed variation is due to the movement of bedload transport in a thin layer near the riverbed. The sediment continuity equation in the bedload layer is expressed by

$$\left(1 - \lambda\right)\frac{\partial z_b}{\partial t} + \left[\frac{\partial q_{bx}}{\partial x} + \frac{\partial q_{by}}{\partial y} \right] = 0 \tag{18}$$

where z_b= riverbed elevation; λ = porosity of sediment on the riverbed; q_{bx} , q_{by} = bedload transport rate in x and y direction, respectively.

The total bedload transport rate is evaluated with the Ashida-Michiue formula as below

$$\frac{q_b}{\sqrt{\left(s-1\right) g d^3}} = 17 \tau_{*e}^{3/2} \left(1 - \sqrt{\frac{\tau_{*c}}{\tau_*}}\right)\left(1 - \frac{\tau_{*c}}{\tau_*}\right) \tag{19}$$

where q_b= bedload discharge per unit width; s= specific gravity of sediment; g= gravitational acceleration; d= diameter of sediment; $\tau_{*e}, \tau_{*c}, \tau_*$ = dimensionless effective shear stress, critical shear stress and shear stress, respectively. The dimensionless shear stress is connected with the squared friction velocity u_*^2 and is defined as

$$\tau_* = \frac{u_*^2}{(s-1) g d} \tag{20}$$

In the calculation of bedload transport in a channel with a relatively gentle slope, the critical shear stress is obtained from the well-accepted Shield's diagram or other popular criteria and the particle gravity does not affect the sediment motion significantly. However, the local bed slope usually becomes much steeper in the situation where local scour occurs. The local bed slope may affect [1] the sediment threshold condition, i.e. the condition just sufficient to initiate sediment motion, and [2] the sediment transport rate and direction once the sediment is in motion. In the conventional treatment, the longitudinal velocity is usually assumed predominant and the local bed slope is resolved into a longitudinal bed and a transverse bed (e.g. van Rijn, 1993 and Duan et al., 2001). However, this kind of treatment is questionable

when applied to the sediment transport around local scour holes where the magnitudes of the three velocity components are almost comparable. In view of these, a new method is proposed herein.

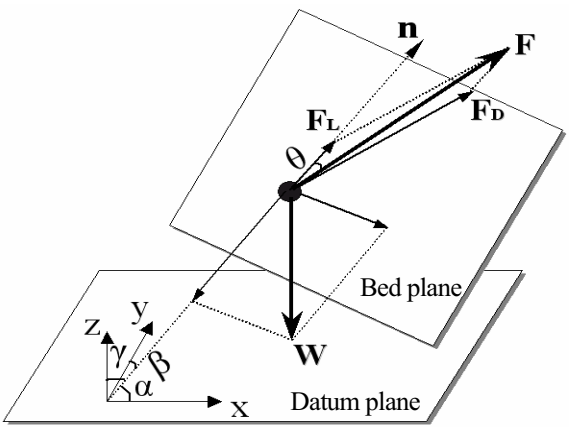

Fig 5 Sediment particle under threshold condition

Take a look at a sediment particle resting on a sloping bed. Under the threshold condition, the forces acting on the particle are shown in Fig.5. Assuming that the Reynolds stress is large enough, all forces act through the particle center. The forces include the submerged weight of the particle **W** and the hydrodynamic force **F**. The latter one is usually resolved into a drag force $\mathbf{F_D}$ tangential to the bed plane and a lift force $\mathbf{F_L}$ normal to the bed plane in the analyses of sediment transport. In the figure, **n** stands for the normal direction of the local bed plane and α, β & γ are the corresponding direction angles (i.e. $\mathbf{n} = \cos\alpha\mathbf{i} + \cos\beta\mathbf{j} + \cos\gamma\mathbf{k}$). Write the hydrodynamic force **F** as the multiplication of its magnitude F and its direction, i.e.

$$\mathbf{F} = F\left(\cos\alpha_1\mathbf{i} + \cos\beta_1\mathbf{j} + \cos\gamma_1\mathbf{k}\right) \tag{21}$$

where α_1, β_1 & γ_1 are the direction angles of the hydrodynamic force **F**. Consequently, the lift force $\mathbf{F_L}$ and the drag force $\mathbf{F_D}$ have the following forms.

$$\mathbf{F_L} = F\cos\theta\left(\cos\alpha\mathbf{i} + \cos\beta\mathbf{j} + \cos\gamma\mathbf{k}\right) \tag{22}$$

$$\begin{aligned}\mathbf{F_D} = F\Big[&\left(\cos\alpha_1 - \cos\theta\cos\alpha\right)\mathbf{i} + \left(\cos\beta_1 - \cos\theta\cos\beta\right)\mathbf{j} \\ &+ \left(\cos\gamma_1 - \cos\theta\cos\gamma\right)\mathbf{k}\Big]\end{aligned} \tag{23}$$

in which θ is the angle between the flow direction and the normal direction of the bed plane and is expressed by

$$\cos\theta = \cos\alpha\cos\alpha_1 + \cos\beta\cos\beta_1 + \cos\gamma\cos\gamma_1 \tag{24}$$

Under the threshold condition, the resulted driving force $\mathbf{F_r}$ is balanced by the stabilizing force $\mathbf{F_s}$. The former reads

$$\begin{aligned}\mathbf{F_r} = &\left[W\cos\gamma\cos\alpha + F\left(\cos\alpha_1 - \cos\theta\cos\alpha\right)\right]\mathbf{i} \\ &+ \left[W\cos\gamma\cos\beta + F\left(\cos\beta_1 - \cos\theta\cos\beta\right)\right]\mathbf{j} \\ &+ \left[-W\sin^2\gamma + F\left(\cos\gamma_1 - \cos\theta\cos\gamma\right)\right]\mathbf{k}\end{aligned} \tag{25}$$

The latter acts in the direction opposite to the driving force and has a magnitude of

$$F_s = \left(W\cos\gamma - F\cos\theta\right)\tan\varphi \tag{26}$$

where φ = angle of sediment repose. Using the equation of force balance, i.e. $F_r = F_s$, one obtains

$$\begin{aligned}&\left(\sin^2\theta - \cos^2\theta\tan^2\varphi\right)F^2 + 2WF\left(l + \cos\gamma\cos\theta\tan^2\varphi\right) \\ &\quad + \left(\sin^2\gamma - \cos^2\gamma\tan^2\varphi\right)W^2 = 0\end{aligned} \tag{27}$$

in which l is expressed by

$$l = \cos\gamma\cos\theta - \cos\gamma_1 \tag{28}$$

The positive solution of Eq.27 is

$$F = \frac{W}{\sin^2\theta - \cos^2\theta\tan^2\varphi}\left[m - \left(l + \cos\gamma\cos\theta\tan^2\varphi\right)\right] \tag{29}$$

in which

$$m = \sqrt{l^2 + \left(\sin^2\theta\cos^2\gamma + \sin^2\gamma\cos^2\theta + 2l\cos\gamma\cos\theta\right)\tan^2\varphi - \sin^2\theta\sin^2\gamma} \tag{30}$$

On the other hand, the submerged particle weight W and the drag force F_D are empirically expressed as follows.

$$W = c_1\left(s - 1\right)\rho g d^3 \quad F_D = c_2\tau_b d^2 \tag{31}$$

where c_1 = coefficient related to the shape of the particle; c_2 = coefficient depending on the local Reynolds number. Normalizing Eq.29 with Eq.31, one has the dimensionless critical shear stress τ_{*c} for an arbitrary sloping bed as follows

$$\tau_{*c} = \frac{\tau_{bc}}{\left(s-1\right)\rho g d} = \frac{c_1}{c_2}\frac{\sin\theta}{\left(\sin^2\theta - \cos^2\theta\tan^2\varphi\right)}\left[m - \left(l + \cos\gamma\cos\theta\tan^2\varphi\right)\right] \tag{32}$$

where τ_{bc} = critical near-bed shear stress.

In case of a horizontal bed (α, β, γ) = (90°, 90°, 0) and the flow parallel to the bed plane $\theta = \gamma_1 = 90°$, Eq.32 becomes

$$\tau_{*c0} = \frac{c_1}{c_2}\tan\varphi \tag{33}$$

where τ_{*c0} = dimensionless critical shear stress for a horizontal bed. As has been mentioned before, this can be easily obtained from some well-tested criteria such as the Shields' diagram. If Eq.33 is introduced into Eq.32, a bed slope factor K is obtained below, expressing the difference in the critical shear stress between on a sloping bed and on a horizontal bed.

$$K = \frac{\tau_{*c}}{\tau_{*c0}} = \frac{\sin\theta}{\left(\sin^2\theta - \cos^2\theta\tan^2\varphi\right)\tan\varphi}\left[m - \left(l + \cos\gamma\cos\theta\tan^2\varphi\right)\right] \tag{34}$$

Eq.34 indicates that the bed slope factor is not only a function of the bed slope and the angle of sediment repose but also a function of the flow direction. If the flow is parallel to the bed plane, it has a simpler form as

$$K = \frac{\sqrt{l^2 - \sin^2\gamma + \cos^2\gamma\tan^2\varphi} - l}{\tan\varphi} \tag{35}$$

This bed slope factor is used in this paper for the model applications. In case of a longitudinal bed slope (denoted as θ_l) and the longitudinal velocity is predominant, i.e. (α, β, γ) = (90°-θ_l, 90°, θ_l) and (α_1, β_1, γ_1) = (θ_l, 0, 90°-θ_l), one has the following bed slope factor

$$K = \cos\theta_l\left(1 - \frac{\tan\theta_l}{\tan\varphi}\right) \tag{36}$$

For a transverse bed slope (denoted as θ_t) and still the longitudinal velocity is predominant, i.e. (α, β, γ) = (90°, 90°-θ_t, θ_t) and (α_1, β_1, γ_1) = (0°, 90°, 90°), one goes to another bed slope factor

$$K = \cos\theta_t\sqrt{1 - \frac{\tan^2\theta_t}{\tan^2\varphi}} \tag{37}$$

It is noted that Eq.36 and Eq.37 or their variants are conventional bed slope factors in the literatures. A simple multiplication of the two factors has been suggested to account for the effect of a combined longitudinal and transverse bed slope although the treatment is physically questionable (e.g. van Rijn, 1993 and Duan et al., 2001). Comparing these two conventional bed slope factors with Eq.35, it is found that the new bed slope factor is more general while still maintains the simplicity for programming.

According to the above analysis process, it is readily to assume that the sediment movement follows the direction of the resulted driving force. Hence the three components of the bedload transport rate are easily obtained from Eq.25.

The three components of the bedload transport rate are mapped onto a 2D mesh covering the bed surface and Eq. 18 is then solved. Consequently, the bed deformation at each time step is obtained. Nevertheless, unrealistic local bed slopes over the angle of sediment repose probably occur in the simulation. This phenomenon should be avoided for non-cohesive beds. A sediment slide process is assumed to take place if the local bed slope becomes too steep. After the slide process, the bed level at each mesh is adjusted and all the local bed slopes are no more than the angle of sediment repose.

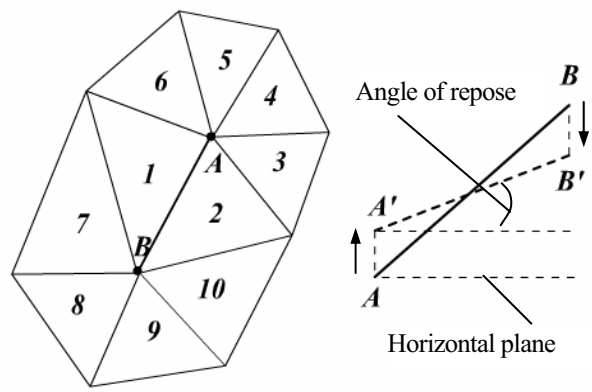

Fig 6 Sediment slide process

A plane-view of the CV (Control volume) surface on the riverbed is shown in Fig. 6 (left). At each time step, the program checks the nodes on the riverbed and the corresponding neighbors. If a slope steeper than the angle of sediment repose has been detected connecting node A (x_A, y_A, z_A) and node B (x_B, y_B, z_B), the elevations of node A and node B should be adjusted to nodes A' and B' as shown in Fig. 6 (right). The change of the elevation is denoted as δz_A and δz_B, respectively. Assuming that the local bed slope connecting nodes A' and B' equals the angle of sediment repose, one has

$$\left(z_B-\delta z_B\right)-\left(z_A+\delta z_A\right)=\tan\varphi\sqrt{\left(x_B-x_A\right)^2+\left(y_B-y_A\right)^2} \quad (38)$$

On the other hand, sediment conservation should be ensured during the adjustment, i.e.

$$\sum S_{A,neighbor}\delta z_A=\sum S_{B,neighbor}\delta z_B \quad (39)$$

where $S_{A,\ neighbor}$ = projected area of the mesh surrounding node A (i.e. mesh 1 to mesh 6 shown in Fig. 6) and $S_{B,\ neighbor}$ = projected area of the mesh surrounding node B (i.e. mesh 1, mesh 2 and mesh 7 to mesh10 in Fig. 6).

With Eq. 38 and Eq. 39, the new locations of node A and node B can be obtained. This process is repeated until the bed slopes connecting all the CV nodes and their corresponding neighbors are not more than the angle of sediment repose.

3.3 Numerical schemes and solution procedure

In a Cartesian coordinate system, the governing equations for the flow have a common form as below.

$$\frac{\partial}{\partial t}\left(h\phi\right)+\frac{\partial}{\partial x}\left(hu\phi\right)+\frac{\partial}{\partial y}\left(hv\phi\right)=\frac{\partial}{\partial x}\left(h\Gamma\frac{\partial\phi}{\partial x}\right)+\frac{\partial}{\partial y}\left(h\Gamma\frac{\partial\phi}{\partial y}\right)+s_\phi \quad (40)$$

where $h\Phi$ = transport quantity (for the momentum equations, such definitions are used for clarity: $M = hu$ and $N = hv$), Γ = diffusive coefficient and $s\phi$ = source term.

Eq. 40 is integrated over a series of CVs (Control volumes) covering the study domain using the FVM (Finite volume method) with a collocated variable arrangement and is then submitted to discretization. The discretization adopts a term-by-term process. For the temporal term, the Euler scheme is employed. The power law scheme is used for the convection and diffusion terms. Surface fluxes are interploated following the method suggested by Rhie and Chow (1983). For the velocity-pressure coupling, the SIMPLER (Semi-implicit method for pressure-linked equation, revised version) procedure proposed by Patankar (1980) is adopted.

After the discretization, momentum equations for M and N at a CV surface have the form as

$$\begin{aligned} a_f M_f &= \sum a_{nb}M_{nb}-\int gh\frac{\partial H}{\partial x}dl\Big|_f+b_f \\ a_f N_f &= \sum a_{nb}N_{nb}-\int gh\frac{\partial H}{\partial y}dl\Big|_f+b_f \end{aligned} \quad (41)$$

where subscript f = the interface between two neighboring CVs; subscript nb = the neighboring CV; a = coefficient of the final discretized equations and b = source term excluding the pressure term. Defining pseudo-variables corresponding to M and N as

$$\hat{M}_f=\frac{\sum a_{nb}M_{nb}+b_f}{a_f} \qquad \hat{N}_f=\frac{\sum a_{nb}N_{nb}+b_f}{a_f} \quad (42)$$

Eq. 41 can be written as

$$M_f=\hat{M}_f-\frac{\int gh\frac{\partial H}{\partial x}dl\Big|_f}{a_f} \qquad N_f=\hat{N}_f-\frac{\int gh\frac{\partial H}{\partial y}dl\Big|_f}{a_f} \quad (43)$$

In the derivation below, the guessed pressure and the velocity component resulted from the momentum equation not satisfying the continuity equation are denoted with an superscript *, the correction of an variable is denoted with an index ‘ and the variable without any superscript stands for the final value, i.e.

$$M=M^*+M' \qquad N=N^*+N' \qquad H=H^*+H' \quad (44)$$

With these definitions and Eq. 41, it is readily to see

$$\begin{aligned} a_f M_f^* &= \sum a_{nb}M_{nb}^*-\int gh\frac{\partial H^*}{\partial x}dl\Big|_f+b_f \\ a_f N_f^* &= \sum a_{nb}N_{nb}^*-\int gh\frac{\partial H^*}{\partial y}dl\Big|_f+b_f \end{aligned} \quad (45)$$

Subtracting Eq.45 from Eq. 41 and taking Eq.44 into account, one obtains the velocity correction

$$\begin{aligned} M'_f &= \frac{\sum a_{nb}M'_{nb}}{a_f}-\frac{\int gh\frac{\partial H'}{\partial x}dl\Big|_f}{a_f} \\ N'_f &= \frac{\sum a_{nb}N'_{nb}}{a_f}-\frac{\int gh\frac{\partial H'}{\partial y}dl\Big|_f}{a_f} \end{aligned} \quad (46)$$

If the first term on the right hand side is omitted, the velocity correction has a simple relationship with the pressure correction. Introducing this relationship into Eq.44, one goes to Eq.47.

$$M_f=M_f^*-\frac{\int gh\frac{\partial H'}{\partial x}dl\Big|_f}{a_f} \qquad N_f=N_f^*-\frac{\int gh\frac{\partial H'}{\partial y}dl\Big|_f}{a_f} \quad (47)$$

It is found that Eq. 47 has almost the same form as Eq.43. In order to assure the mass conservation, the continuity equation for each CV should be satisfied, i.e.

$$\int\frac{\partial H}{\partial t}\Big|_P+\sum\left(M_f l_x+N_f l_y\right)=0 \quad (48)$$

where subscript P = the present approximated CV;

Substituting Eq.43 and Eq.47 into Eq.48, one has the

so-called pressure equation and pressure-correction equation for H and H', respectively. The calculation sequences are therefore outlined as follows.

[1] Calculate the coefficients in the momentum equations. Omit the pressure term and solve for the pseudo-velocities.

[2] With the pseudo-velocities, the pressure equation is solved. This leads to the water stage and water depth.

[3] Based on the resulted water stage, solve the momentum equations to get the approximated velocity components.

[4] The resulted velocity components are used to calculate the mass fluxes through CV faces with the Rhie-Chow interpolation method. Solve the pressure-correction equation to obtain the pressure correction.

[5] From the pressure correction, the velocity correction is obtained. And correct the velocity field.

[6] Solve the transport equations for the turbulence kinetic energy and its dissipation rate, respectively. And then update the eddy viscosity.

[7] Repeat the above procedures until the residual level becomes sufficiently small or the prescribed maximum iteration step number is covered.

At the dry-wet boundary, the surface fluxes are not properly estimated with any linear interpolation method due to the steep gradient of the pressure. Furthermore, the zero velocity and water depth at the center of the dry CV bring numerical problems when calculating the velocity correction by using the pressure correction. Hence some additional treatments are needed between step [4] and step [5] to account for the dry-wet boundary.

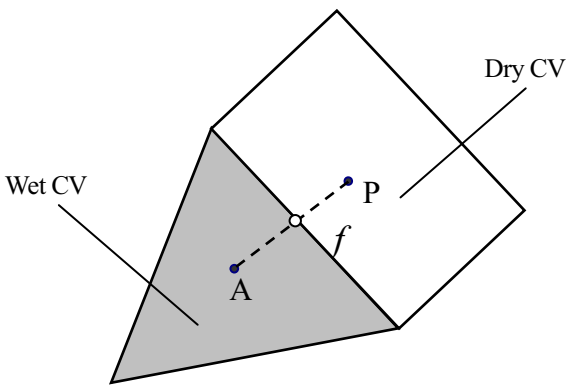

Fig. 7 Treatment of the dry-wet boundary

The pressure correction in Step [4] is firstly used to correct surface fluxes (denoted with subscript *new*) around dry CVs (Fig.7), i.e.

$$M^*_{f,new}=M^*_f-\frac{1}{a_f}gh\left(H'_A-H'_P\right)l_x \quad N^*_{f,new}=N^*_f-\frac{1}{a_f}gh\left(H'_A-H'_P\right)l_y \tag{49}$$

where subscript A = the adjacent CV (i.e. wet CV) and l_x, l_y = projected length of the dry-wet boundary. The new fluxes are then introduced into Eq.47. Considering Eq.48 for mass conservation, a new pressure correction for the dry CV is

$$H'_P=\frac{ghH'_A\sum\frac{l^2}{a_f}-\sum\left(M^*_{f,new}l_x+N^*_{f,new}l_y\right)}{ghH'_A\sum\frac{l^2}{a_f}+A_P/\Delta t} \tag{50}$$

where A_p = area of present CV (i.e. dry CV) and Δt= time step.

Since the dry CV has a zero water depth in the previous time step, the pressure correction gives the new water stage directly. Other quantities such as a_p at the center of the dry CV can be estimated by linear interpolation from the surface values. Hence the dry CV can be treated as a common CV. Then program goes to step [5] with the updated pressure correction. This treatment is found to provide an effective way to account for the water edges shifting without significant increasing of computational cost.

3.4 Boundary conditions

In actual river conditions, the boundaries generally include the inlet, outlet and solid walls. The hydrograph is usually known at the inlet boundary. Hence, the velocity is prescribed there and is estimated according to the local conveyance. If the discharge is normal to the inlet, then

$$\bar{u}_{in}=K\frac{h^{2/3}}{n} \quad \text{where} \quad K=\frac{Q}{\sum\frac{h^{5/3}}{n}l} \tag{51}$$

in which $\bar{u}_{in}$ = velocity at each inlet mesh; Q = total discharge at a time step; n =Manning's roughness coefficient and l = length of the inlet boundary. The turbulence kinetic energy k is related to the velocity $\bar{u}_{in}$ and the turbulence intensity I via $k=1.5\bar{u}_{in}I^2$. The dissipation rate ε is estimated from Eq.10 by specifying a viscosity ratio (ν_t/ν) around 10-20.

At the outlet, a zero gradient boundary is assumed there. Moreover, an *ad hoc* treatment is applied to correct the velocity components in order to assure the global mass conservation, i.e.

$$u_{out} = \frac{Q_{in}}{Q_{out}} u^{old} \qquad v_{out} = \frac{Q_{in}}{Q_{out}} v^{old} \tag{52}$$

in which the discharge Q with subscripts *in* and *out* is the total discharge computed at the inlet and outlet boundaries, respectively. The velocity component with a superscript *old* stands for the computed value before correction. It is noted that Eq.52 provides a direct way to correct the velocity at the outlet. Therefore, there is no need to correct the outlet velocity again in the SIMPLER procedure.

At solid walls such as channel banks and emerged hydraulic structures, the wall function approach is used for the computational convenience. However, the boundaries between wet and dry CVs are not treated as solid walls as has been mentioned in the previous contexts.

4. Results and discussions

Selected results are presented in this section to further the understanding of channel morphodynamics around groins and to seek design methods for groins in river restoration. Firstly, the flow field and bed deformation process around the two existing groins during a typical flood season in 2005 is investigated. After that, the bed deformation characteristics in two different cases (with groins and without groins) are compared under the same water discharges and sediment conditions. The simulation is based on the experimental scale, but all the results have been transformed to prototype scale for clarity.

4.1 Bed deformation in a flood process

The bed evolution process during a flood in September 2005 is investigated here. The flood is simplified to a 3-stage process: pre-peak (0~12.2h), peak (12.2~18.7h) and post-peak (18.7~24.5h). At each stage, water discharge and sediment discharge are assumed constant. According to the hydrograph and calibrated sediment discharge by preliminary experiments, the modelled flood process is shown in Fig.8. Hybrid unstructured mesh is used in the computation for a better resolution. Part of the mesh system is shown in Fig.9.

From Fig. 10 to Fig. 13, the simulated bed evolution process has been plotted. The flood discharges almost trigger sediment movement in the whole channel. Deposition of sediment in the upstream part of the big sandbar has increased the sandbar height obviously. Moreover, the stream way on the right side of the channel is almost colonized by the head of the sandbar. The local scour at the head of the impermeable groin is filled with sediment transported from upstream. Behind the impermeable groin, the bed is degraded significantly. This is due to the flow separation as well as overtopping. These observations suggest that flood conditions should be prudently considered in groin designs.

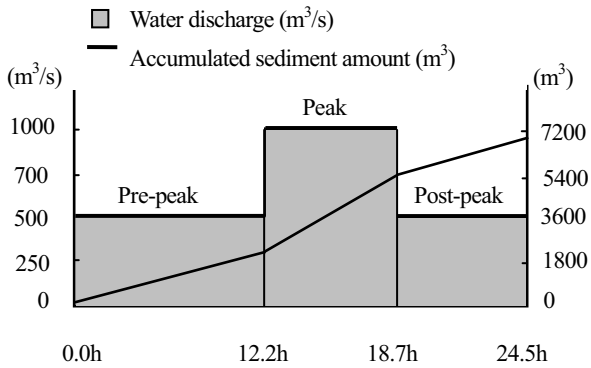

Fig 8 Modeled flood process

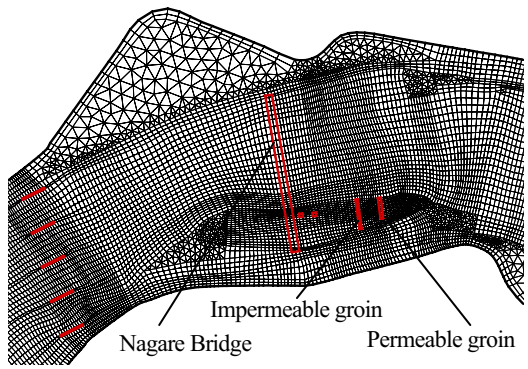

Fig 9 Hybrid mesh system

Fig.13 and Fig.14 show the final bed contour after the flood process according to computation and experiment, respectively. Compared with the bed contour before flood as given in Fig.10, the bed morphology exhibits significant changes after the flood. Both the computation and experimental results indicate that the scour-deposition morphology around the impermeable groin is destroyed. In some area, the scour and bed degradation seem to be under-estimated. It is probably caused by the under-estimation of the effect of the vertical velocity component, which contributes a lot to the sediment transport inside of scour holes and around groins.

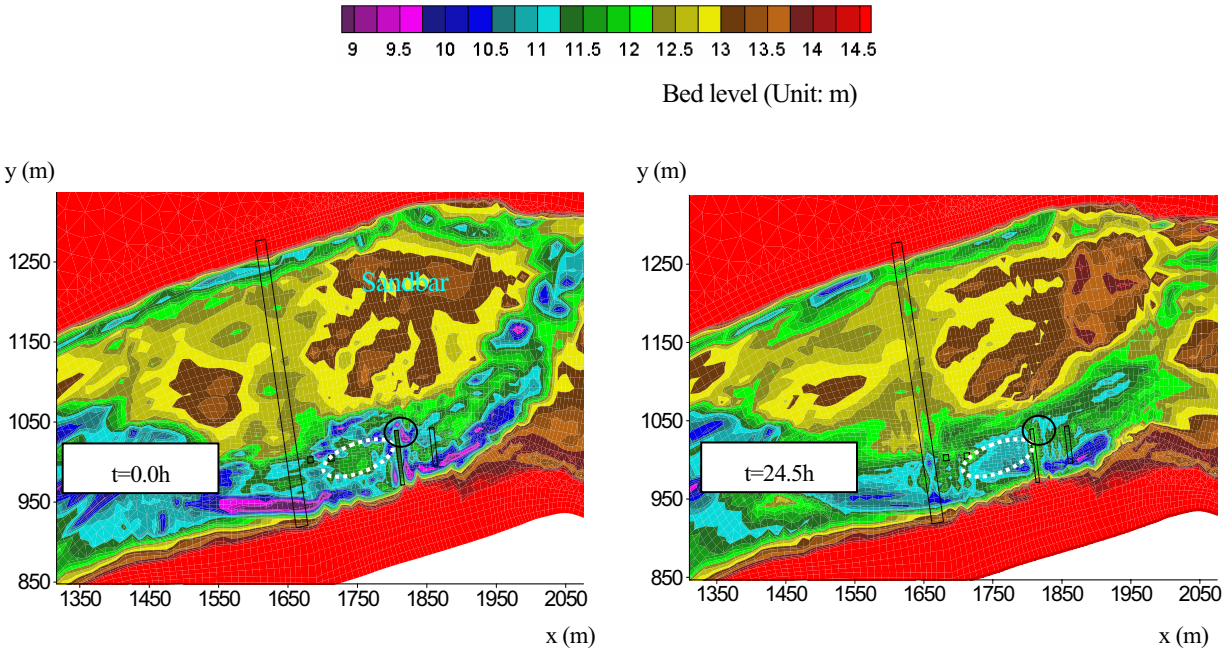

Fig. 10 Initial bed contour

Fig. 13 Final bed contour (Simulation)

Fig.11 Bed contour before peak (Simulation)

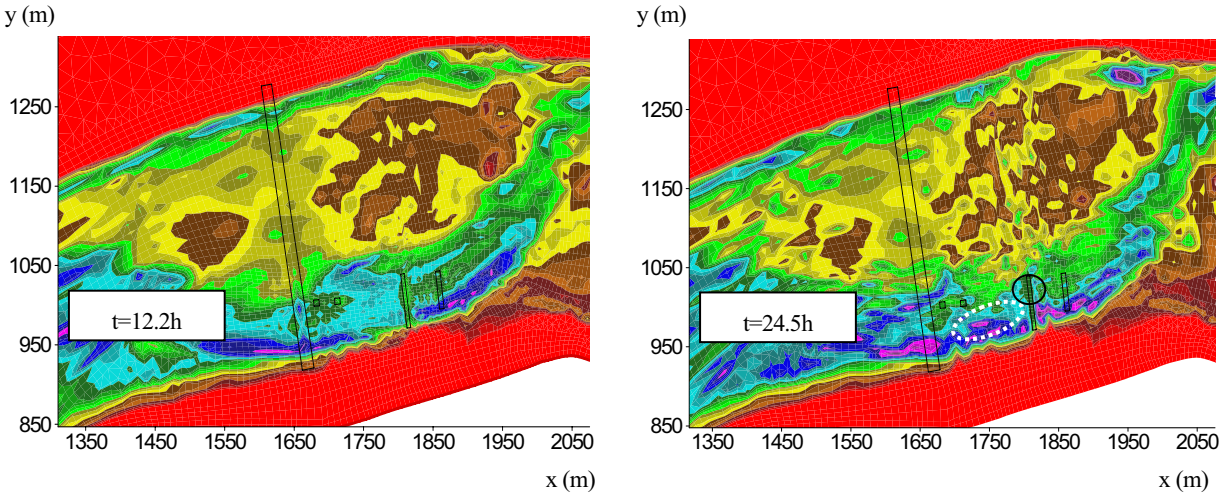

Fig.14 Final bed contour (Experiment)

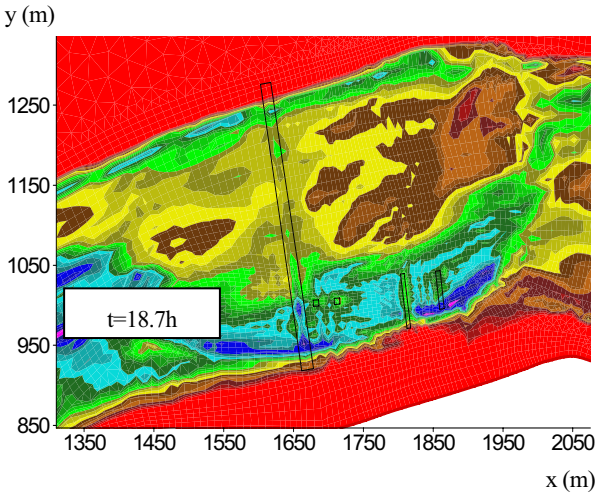

Fig.12 Bed contour after peak (Simulation)

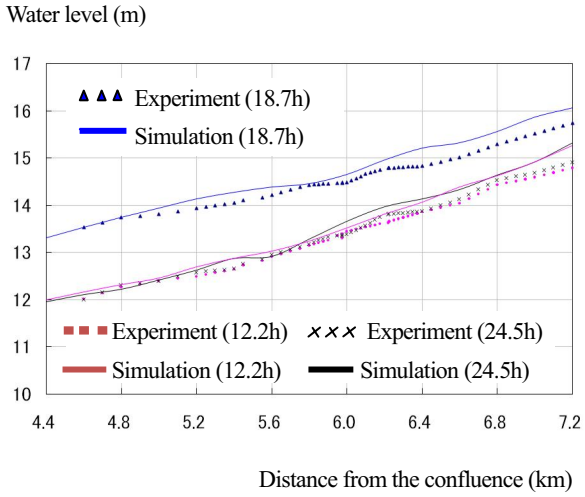

Fig.15 Water level in the flood process

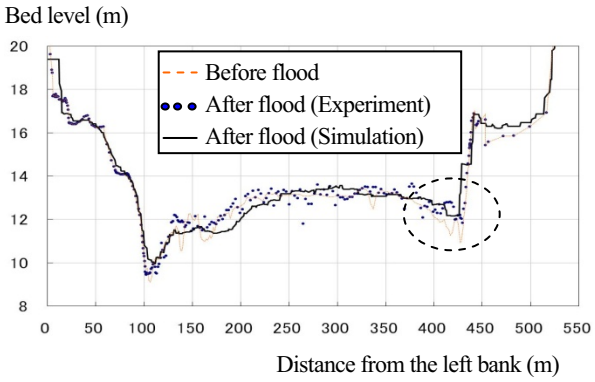

Fig. 16 Bed level before permeable groin (6.2km)

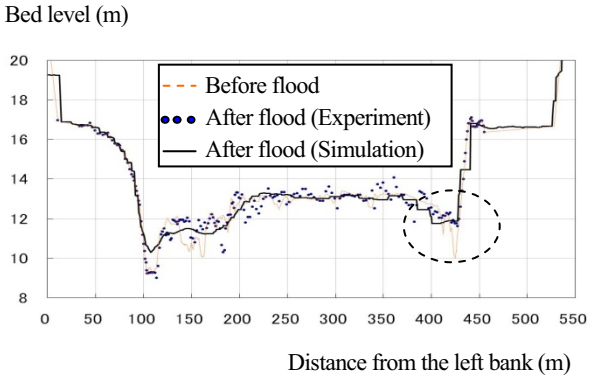

Fig. 17 Bed change between the two groins (S1)

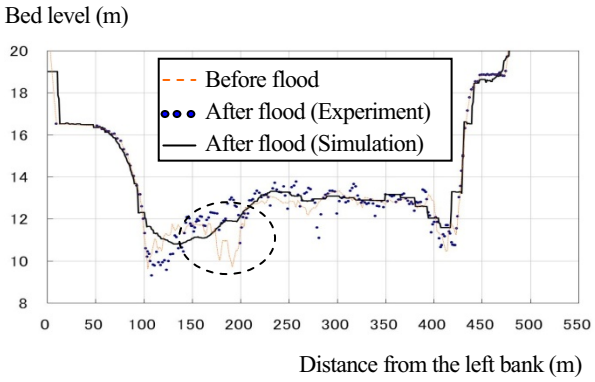

Fig. 18 Bed change after impermeable groin (S2)

The bed deformation at typical transverse sections is shown from Fig.16 to Fig.18. The locations of the sections are depicted in Fig.3. Due to the wavy bed of ripples, the measured bed profiles exhibit great irregularity. Irrespective of this, the computational result is quite encouraging. Fig.18 deserves special attention. Again, the scour-deposition pattern (i.e. pool-riffle morphology) caused by the impermeable groin before the flood is found to be destroyed during the flood. It gives quantitative evidence to previous observations in the change of the bed contour.

The computed water levels along the centerline of the low flow channel are compared with those of the experiments as shown in Fig. 15. In general, water levels exhibit no significant differences at the end of the pre-peak stage (12.2h) and at the end of the post-peak stage (24.5h). Higher water level is observed at the end of the peak (18.7h) due to the higher flood discharge. Simulation results are in reasonable agreement with those of the experiments. Nevertheless, slight over-estimation is found upstream, in particular under the peak discharge. It may be attributed to the use of the same set of Manning's roughness coefficients. The development of ripples and its effect on the bed resistance are not accurately accounted for in the model. The roughness, in the upstream area and in case of higher discharges, has probably been over-estimated.

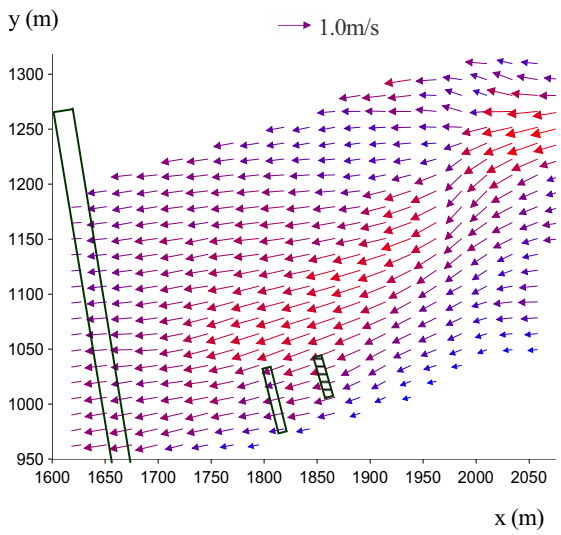

Fig. 19 Surface velocity (Experiment, t=18.7h)

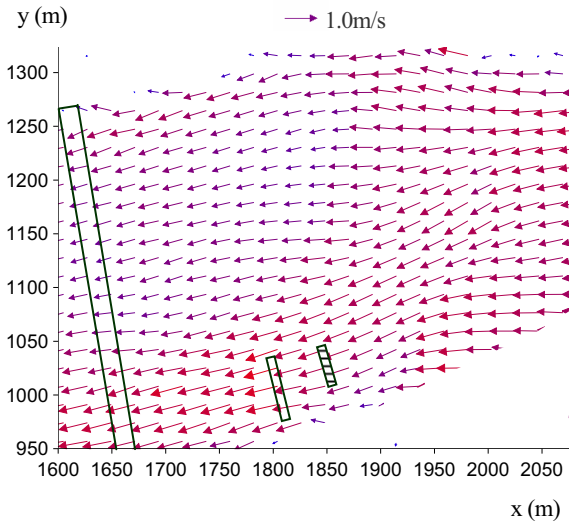

Fig.20 Mean velocity (Simulation, t=18.7h)

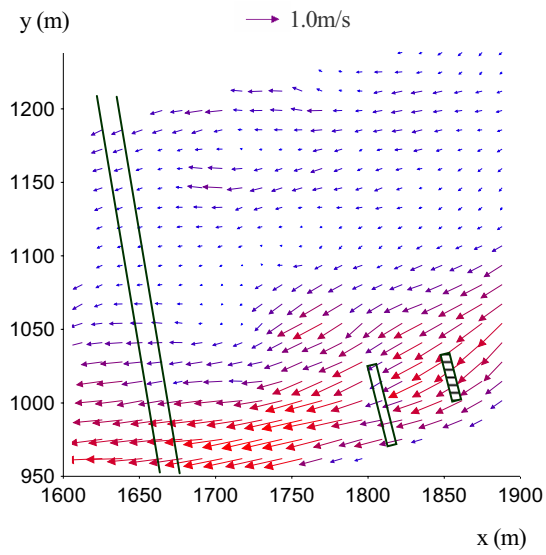

Fig.21 Surface velocity (Experiment, t=24.5h)

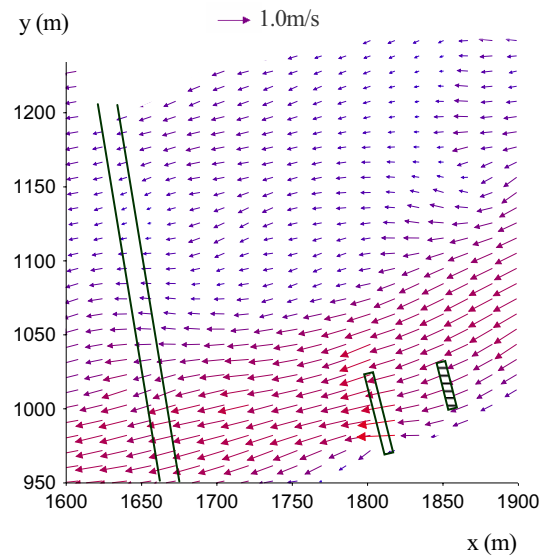

Fig.22 Mean velocity (Simulation, t=24.5h)

The surface velocities were measured in the experiment considering the shallowness of the river flow. The surface velocities around groins at the end of the flood peak (18.7h) and at the end of the flood (24.5h) are shown in Fig.19 and Fig.21, respectively. The computed mean velocities at corresponding time are also plotted in Fig.20 and Fig.22. It was found that the measured surface flow patterns are quite similar to the computed mean flow patterns. The flow fields are closely related to the bed morphologies and water depths. The high velocity zone basically follows the river thalweg. Since the groins are submerged during the flood, they do not have significant influence on the flow directions. However, the flow was accelerated around the groins, in particular the impermeable one. At the end of the flood, one may observe some area where the flow is almost stagnant in the experimental result (Fig.21). However, this phenomenon is not well predicted with the model (Fig.22). The over-estimation of the water level as depicted in Fig.15 is probably responsible for this discrepancy. The bed forms change under different flow, sediment and bed conditions, whose effects on the bed roughness necessitate quantitative estimation. This should be included in the future research.

4.2 Bed deformation in cases with/without groins

In order to investigate the impacts of groins on the channel morphodynamics, experiments with and without groins have been carried out. Considering the importance of flood discharges in the design of groins, cases under flood discharges are selected and presented in this section, which are detailed in Table 1.

Table 1 Selected experimental conditions

Cases	Discharge (m^3/s)	Groins	Time (hour)
1	2000	Yes	16
2	2000	No	16
3	500	Yes	80
4	500	No	80

The flood discharges $2000m^3/s$ and $500m^3/s$ correspond to the maximum annual discharge and the dominant discharge of the river, respectively. The bed contours before the flood and after the flood are plotted from Fig. 23 to Fig. 34 according to the experimental and simulation results.

In case of flood discharge of $2000m^3/s$, the numerical results give very obvious evidence that the groin structures are effective for the bank protection. Comparing Fig. 24 with Fig. 27, one may observe several scour in the area where the groins are removed. Unfortunately, the groins do not show advantages in creation of deposition area in desired locations. This is probably caused by the over-topping flow during the flood.

Similar conclusions may be drawn from the results in case of discharge of $500m^3/s$ (Fig. 29 to Fig. 34). However, the movement of sandbars and development of bed forms under bigger discharge (Case1 and Case2) are much more significant compared with those under smaller discharge (Case3 and Case4).

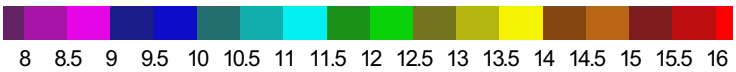

Bed level (Unit: m)

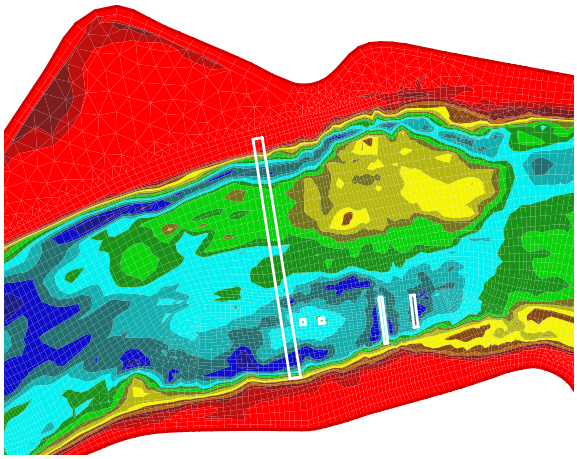

Fig.23 Bed contour (Case1, t=0h)

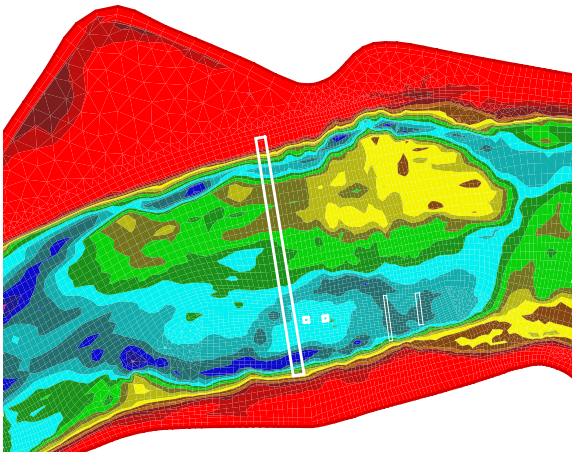

Fig.26 Bed contour (Case2, t=0h)

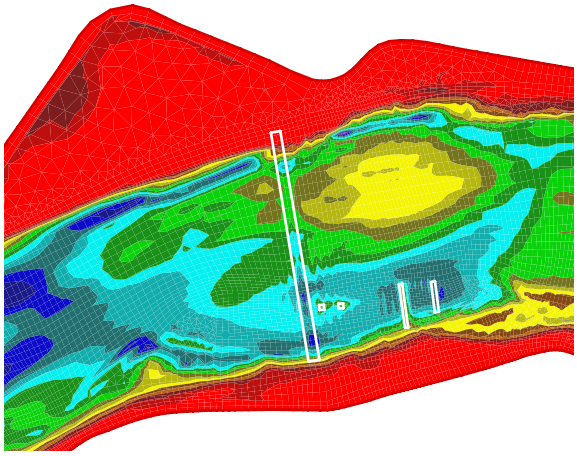

Fig.24 Bed contour (Case1, t=16h, Simulation)

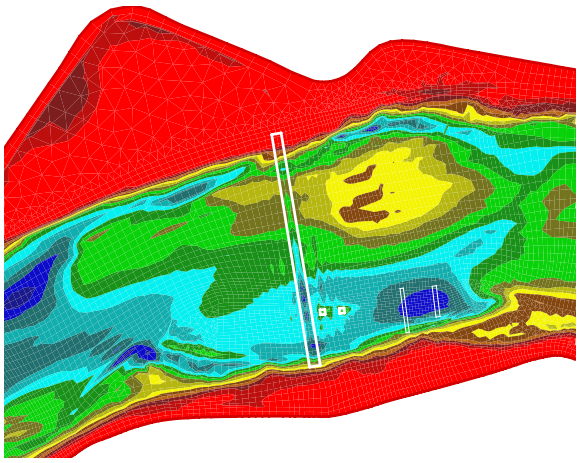

Fig.27 Bed contour (Case2, t=16h, Simulation)

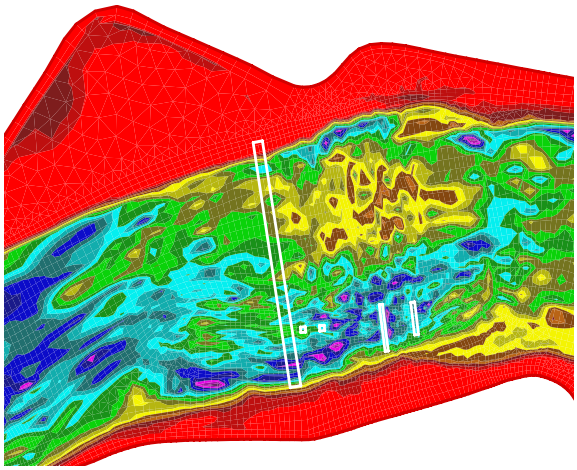

Fig.25 Bed contour (Case1, t=16h, Experiment)

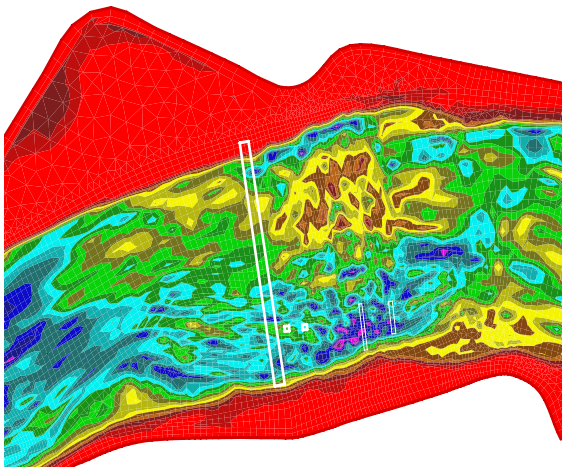

Fig.28 Bed contour (Case2, t=16h, Experiment)

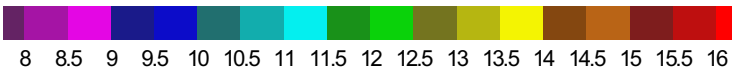

Bed level (Unit: m)

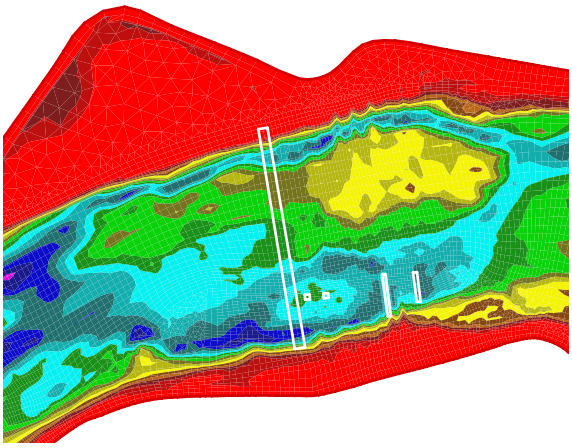

Fig.29 Bed contour (Case3, t=0h)

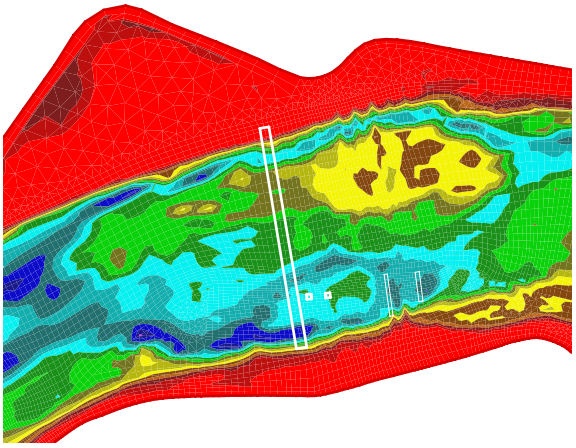

Fig.32 Bed contour (Case4, t=0h)

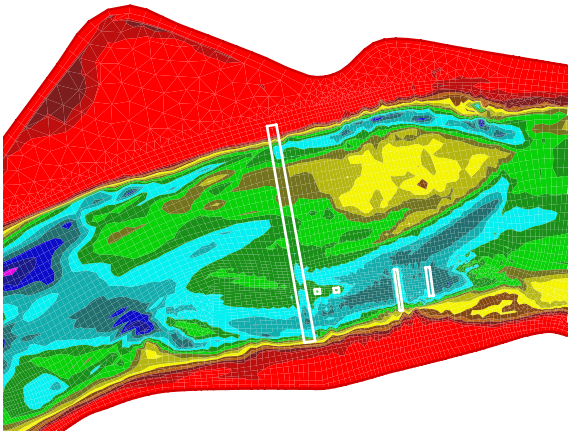

Fig.30 Bed contour (Case3, t=80h, Simulation)

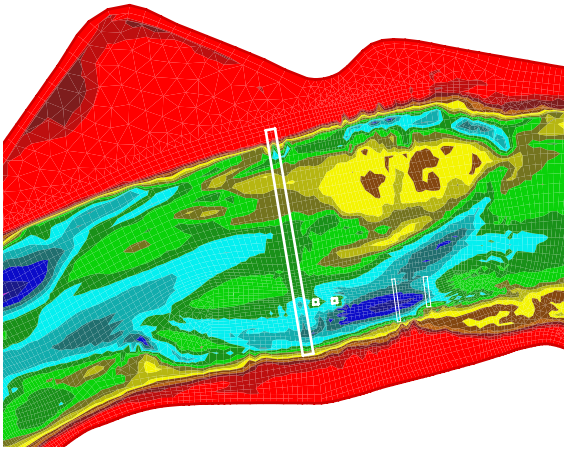

Fig.33 Bed contour (Case4, t=80h, Simulation)

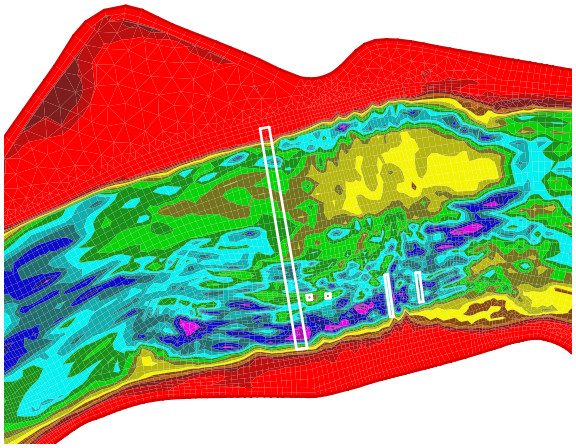

Fig.31 Bed contour (Case3, t=80h, Experiment)

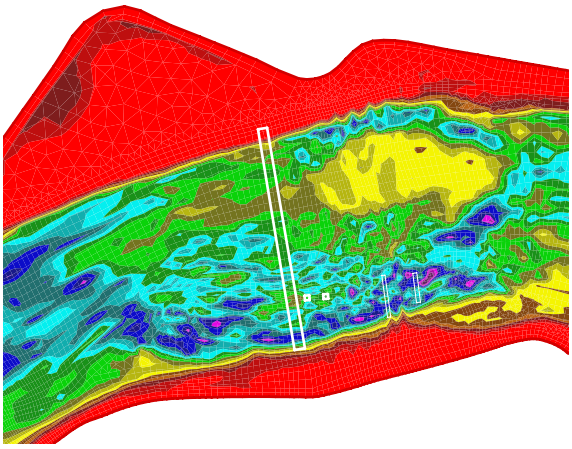

Fig.34 Bed contour (Case4, t=80h, Experiment)

5. Conclusions

This paper presents some results of a research work on the channel morphodynamics due to the construction of groins with both experimental and numerical methods. The experiment is based on a large-scale physical model and is able to resolve the local flow and bed deformation process with a high accuracy. The numerical model takes into account the effects of secondary flows and local bed slopes on the flow and sediment transport. Unstructured meshes are employed in the discretization process of the governing equations, making possible the accurate resolution of commonly encountered complex geometries in actual river conditions. The numerical results have been compared with those of the experimental measurements and reasonable agreements have been obtained.

Compared with most of the existing researches for simplified channels and groin structures under idealized flow and sediment conditions, the results of this research are of practical value. These results may be expected to provide important information for the sustainable design of groin structures. However, comparisons between the experimental and numerical results are not enough yet. Numerical simulations based on the prototype scale as well as the long-term monitoring of the project are a crucial consideration in the next step. Development of a 3D model is also of great need to resolve the detailed flow structure and sediment movement around groins.

Acknowledgements

The authors are grateful to Dr. Yasuyuki Baba and Mr. Akira Nakanishi, who provide a lot of advices and conveniences for the numerical simulations. Mr. Michinari Tani and Mr. Hirokazu Ikeda are also sincerely acknowledged. Without their expertise and kindness, the experimental data and analyses would not be possible.

References

Ashida, K. and Michiue, M. (1972): Studies on bed load transportation for nonuniform sediment and river bed variation. Disaster Prevention Research Institute Annuals, Kyoto Univ., No.14B, pp. 259-273. (in Japanese)

Duan, J.G., Wang, S.S.Y. & Jia, Y. (2001): The application of the enhanced CCHE2D model to study the alluvial channel migration processes, Journal of Hydraulic Research, IAHR, Vol. 39, No. 5, pp. 1-12.

Engelund, F. (1974): Flow and bed topography in channel bends, Journal of the Hydraulics Division, ASCE, Vol. 100, No. HY11, pp. 1631-1648.

Kuhnle, R.A., Alonso, C.V. and Shields, F.D.Jr. (2002): Local scour associated with angled spur dikes. Journal of Hydraulic Engineering, ASCE, Vol.128, No. 12, pp.1087-1093.

Minh Duc, B., Wenka, T. and Rodi, W. (2004): Numerical modeling of bed deformation in laboratory channels, Journal of Hydraulic Engineering, ASCE, Vol.130, No.9, pp.894-904.

Muto, Y., Kitamura, K., Khaleduzzaman, A.T.M. and Nakagawa, H. (2003): Flow and bed topography around impermeable spur dykes, Advances in River Engineering, JSCE, Vol.9. (in Japanese)

Nagata, N., Hosoda, T., Nakato, T. and Muramoto, Y. (2005): Three-dimensional numerical model for flow and bed deformation around river hydraulic structures, Journal of Hydraulic Engineering, ASCE, Vol. 131, No. 12, pp. 1074-1087.

Nanbu, Y. (2007): Experimental Study on the Restoration of Channel Morphology with Groins around the Kouzuya Bridge on the Kizu River, Bachelor's Thesis, Kyoto University, Kyoto, Japan. (in Japanese)

Patankar, S.V. (1980): Numerical Heat Transfer and Fluid Flow, McGraw-Hill, New York.

Rhie, C.M. and Chow, W.L. (1983): Numerical study of the turbulent flow past an airfoil with trailing edge separation, Journal of AIAA, Vol. 21, pp. 1525-1532.

Rodi, W. (1980): Turbulence Models and Their Application in Hydraulics - a State of the Art Review, University of Karlsruhe, Karlsruhe, Germany.

Shields, F. D. Jr., Cooper, C.M. and Knight, S.S. (1995): Experiment in stream restoration, Journal of Hydraulic Eng., ASCE, Vol.121 (6), pp.494-502.

Shimizu, Y. and Itakura, T. (1991): Calculation of flow and bed deformation with a general non-orthogonal coordinate system, Proc. 24 IAHR Congress, Madrid, C-2, pp. 241-248.

Sukhodolov, A., Engelhardt, C., Kruger, A. and Bungartz, H. (2004): Turbulent flow and sediment distributions in a groyne field. Journal of Hydraulic Engineering, ASCE, Vol.130, No. 1, pp.1-9.

Touchi, D. (2006): Investigation of Bed Evolution

around Spur Dykes with Large Scale Physical Model Experiments, Bachelor's Thesis, Kyoto University, Kyoto, Japan. (in Japanese)

van Rijn, L.C. (1993): Principles of Sediment Transport in Rivers, Estuaries and Coastal Seas, AQUA Publications, Amsterdam, The Netherlands.

Zhang, H., Nakagawa, H., Muto, Y., Touchi, D. and Muramoto, Y. (2006): 2D numerical model for river flow and bed deformation based on unstructured mesh, Journal of Applied Mechanics, JSCE, Vol. 9, pp. 783-794.

水制を有する河道の河床変動に関する研究とその河川再生への応用

張　浩・中川　一・武藤　裕則・村本　嘉雄*・當内　大三郎**・南部　泰範**

*京都大学名誉教授

**京都大学大学院工学研究科

要　旨

本研究では，河川再生事業で設置された水制工周辺の流れと河床変動に関して，移動床実験と数値シミュレーションを行った。1/65 スケールの大規模模型水路を用いた水理実験では，局所的な流れと土砂移動現象が，十分な精度で再現できた。数値モデルでは，非構造格子を用いることによって，実河川のような複雑な地形や構造物の形状を適切に表現することが可能になった。本研究で開発した数値モデルを水理実験の流れに対して適用したところ，ほぼ満足な精度で流況と河床変動を再現することが示された。

キーワード: モルフォダイナミクス，水制，河川再生，大規模水理実験，複雑境界，非構造格子